Laser Measurements and Modeling of Shock Tunnel Freestream Velocity and Multi-Species Thermal Nonequilibrium

Elijah R. Jans*, Kyle P. Lynch**, Ross M. Wagnild§, William E. Swain†, Charley R. Downing‡
Sandia National Laboratories, Albuquerque, NM 87123

Jonathan J. Gilvey¶ and Christopher S. Goldenstein††
Purdue University, West Lafayette, IN 47907

Sean P. Kearney¶¶, and Justin L. Wagner‡‡
Sandia National Laboratories, Albuquerque, NM 87123

Coherent anti-Stokes Raman scattering (CARS) and nitric oxide molecular tagging velocimetry (NO-MTV) were used to characterize the freestream in Sandia's Hypersonic Shock Tunnel (HST) using a burst-mode laser operated at 100-kHz. Experiments were performed at nominal freestream velocities of 3 and 4 km/s using both air and N_2 test gas. The CARS diagnostic provides nonequilibrium characterization of the flow by measuring vibrational and rotational temperatures of N_2 and O_2, which are compared to NO temperatures from separate laser absorption experiments. Simultaneous, colinear freestream velocities were measured using NO MTV along with Pitot pressure measurements. This extensive freestream dataset is compared to nonequilibrium CFD that is capable of modeling species-specific, vibrational temperatures throughout the nozzle expansion. Significant nonequilibrium between vibrational and rotational temperatures were measured at each flow condition. N_2 exhibits the most nonequilibrium followed by O_2 and NO. The CFD model captures this trend, although it consistently overpredicts N_2 and O_2 vibrational temperatures. At 3 km/s, the modeled NO nonequilibrium is underpredicted, whereas it is overpredicted at 4 km/s. Good agreement is seen between CFD and the velocity and rotational temperature measurements. Experiments with water added to the test gas yielded no discernable difference in vibrational relaxation.

I. Introduction

Reflected shock tunnels [1] are an excellent tool for studying high-temperature, hypersonic problems such as boundary layer transition [2], ablation [3, 4], and shock-induced flow separation [5]. These phenomena are known to be sensitive to the thermochemical state of the tunnel freestream [6, 7]. Although shock tunnels are a mature technology, much uncertainty in the tunnel freestream conditions remains. The temperature behind the reflected shock wave in the plenum results in dissociation of diatomic species, such as O_2, and the production of additional species, such as nitric oxide (NO). The subsequent rapid expansion through the nozzle results in pronounced thermodynamic

Presented as Paper 2024-1753 at the AIAA SciTech 2024 Forum, Orlando, FL, January 8–12

* – Senior Member of the Technical Staff, Engineering Sciences Center, erjans@sandia.gov. Member AIAA
** – Principal Member of the Technical Staff, Engineering Sciences Center. Senior Member AIAA
§ – Principal Member of the Technical Staff, Engineering Sciences Center. Senior Member AIAA
† – Engineering and Operations Staff, Engineering Sciences Center. Member AIAA
‡ – Principal Technologist, Engineering Sciences Center
¶ – Graduate Student, School of Mechanical Engineering, 585 Purdue Mall, West Lafayette, IN 47907. Member AIAA
†† – Associate Professor, School of Mechanical Engineering, 585 Purdue Mall, West Lafayette, IN 47907. Senior Member AIAA
¶¶ – Distinguished Member of the Technical Staff, Engineering Sciences Center. Associate Fellow AIAA
‡‡ – Distinguished Member of the Technical Staff, Engineering Sciences Center. Associate Fellow AIAA

nonequilibrium where the vibrational temperature, T_v, of diatomic molecules can be much higher than the translational, T_t, and rotational temperature, T_r, at the nozzle exit. Moreover, the chemistry during the expansion can also remain 'frozen' where the freestream maintains a chemical composition having NO and high concentrations of atomic species akin to that in the nozzle throat [8]. Additionally, the T_v at the nozzle exit may vary between species [9], but models to predict these differences remain unvalidated. Detailed multi-species, multi-temperature measurements are therefore required to inform and validate predictive models for the nozzle expansion process and characterize the test section freestream.

The millisecond test times, high background emission, and low freestream densities in shock tunnels make measurements challenging. Early attempts at laser diagnostics including laser-induced fluorescence (LIF) [10], MTV [11], and CARS [12] measured freestream parameters, but only at a single instance within a run. Parker et al. [13] used laser absorption spectroscopy (LAS) in the CUBRC LENS I reflected shock tunnel to measure NO concentration and found CFD to overpredict NO mole fractions by approximately a factor of three. The same group later found LAS freestream velocity measurements to be in good agreement with CFD for velocities under approximately 3700 m/s [14]. More recently, Finch et al. [15] used high-speed LAS to measure the temporal evolution of NO T_r, T_v, concentration, and freestream velocity in the California Institute of Technology T5 reflected shock tunnel. The velocities were found to be in good agreement with nozzle code simulations, whereas NO was found to be much closer to thermal equilibrium than predicted. Concurrent measurements indicated the water content varied between experiments; a potentially important observation given that water produces faster vibrational relaxation [16].

Gross and Schwartzentruber [17] combined a nonequilibrium nozzle flow model with the NO data from the T5 experiments to characterize the freestream. The model accounted for thermal nonequilibrium but assumed a constant T_r and T_v across species. The authors demonstrated the presence of helium, a driver gas contaminant [18], could substantially decrease the freestream rotational temperature while to a lesser extent increase the freestream velocity.

Recent advances in frequency-tunable, burst-mode laser diagnostics [19] have enabled time-resolved CARS measurements [20] of homonuclear molecular temperatures typically inaccessible with LAS and is spatially resolved rather than path integrated. The current paper investigates N_2 and O_2 rotational and vibrational temperatures in the air freestream of the HST [21], while comparing to complimentary measurements of NO rotational and vibrational temperatures acquired using LAS detailed in Gilvey et al. [22]. Additionally, simultaneous freestream velocity measurements were performed using NO MTV along with concurrent measurement of stagnation and Pitot pressures.

Experiments were performed using bottled "synthetic" air (80% N_2, 20% O_2) and ambient air to explore the effects of water on vibrational relaxation. Experiments with nitrogen test gas were also performed to decouple chemical reaction effects from thermal relaxation. In this work, repeated runs were performed at multiple flow conditions to elucidate meaningful trends and assess repeatability in the impulse facility. The measurements are then compared to species-specific thermal nonequilibrium predictions with the Sandia Parallel Aerodynamics and Reentry Code (SPARC) [23].

II. Experimental Configuration

A. HST

The HST at Sandia National Laboratories is a research-scale, free-piston facility capable of producing high-enthalpy hypersonic flow with freestream velocities ranging from 3 to 5 km/s [21]. A free-piston shock tube generated the high temperature and pressure stagnation reservoir gas for the shock tunnel. The driver gas was a mixture of helium and argon compressed using a 35-kg piston. Cruciform-scored diaphragms separated the driver and driven sections of the shock tube, and a 5-cm orifice plate was used to control piston motion during the burst. Along the driven section were six high-speed pressure transducers (PCB 113B24, 6.9 MPa range) to measure the incident shock speed U_s.

A thin secondary diaphragm separated the shock tube from the nozzle. The nozzle had a throat diameter of 12.7 mm, with a circular throat cross-section blended to a conical expansion of 7.9 degrees. The area ratio was 784 corresponding to a 35.6-cm exit diameter. The flow from the nozzle exhausted into a test section with a diameter of 0.5 m and length of 1.4 m, connected to a vertical dump tank initially evacuated to approximately 25 Pa. The core-flow diameter, as determined by a Pitot rake, was approximately 25 cm. The side walls of the test section used 25-cm diameter uncoated UV fused silica window ports for laser diagnostics. Pitot pressures were measured using a rake containing 17 sensors located a distance 23 cm from the nozzle exit. The rake was instrumented with alternating PCB 113B27 and 113B28 sensors (689 and 344 kPa range, respectively). Each was fitted with a front 'swirl' cap that shielded the sensor from direct exposure to optical radiation [24]. Pitot pressure measurements presented herein are time-averages of the five inner 113B28 sensors within the core flow.

HST experiments were performed at four conditions with the pre-shot design parameters listed in Table 1. The driver section was operated to produce freestream velocities of nominally 3 km/s and 4 km/s by adjusting driver gas He/Ar ratio. Before the run, the driven section was pulled down to vacuum and backfilled with either synthetic air (80% N_2, 20% O_2), "humid air" from the laboratory, or pure N_2. To ensure purity of the driven gas, the shock tube was evacuated to ~50 mTorr and purged with the test gas a total of six times prior to filling to the final shock tube initial pressure.

Table 1: HST Condition Design Parameters.

Condition	Compressor He/Ar Mole Fraction [-]	Compressor Pressure [kPa]	Reservoir Pressure [MPa]	Shock Tube Pressure [kPa]	Burst Pressure [MPa]
3 km/s - Air	80/20	86	2.58	53	18.2 ± 0.8
3 km/s - N_2	80/20	86	2.58	53	17.1 ± 1.2
4 km/s - Air	96/4	77	2.90	17	23.3 ± 0.2
4 km/s - N_2	96/4	77	2.90	17	23.6 ± 0.3

Measured and calculated conditions in the stagnation chamber of the reflected shock tunnel are described in Table 2. The stagnation pressure, P_0, was measured with a PCB 113B22 (34.5 MPa range) sensor located 54 mm upstream of the nozzle entrance as reported in Table 2. The stagnation pressure uncertainty corresponds to the time-average of the uncertainty during the quasi-steady test time of the shock tunnel, defined in Section IV. The stagnation temperature, T_0, and total enthalpy, H_0, were estimated from the reflected shock conditions given by the NASA Chemical Equilibrium with Applications (CEA) [25]. Here CEA was run in "shock" mode using the measured incident shock speed and pre-shot test gas conditions. The uncertainties in the CEA predictions correspond to propagation of uncertainties in the measured U_s.

Table 2: HST Shock Tube and Stagnation Conditions.

Condition	Shock Speed U_s (km/s)	Stagnation Pressure P_0 (MPa)	Stagnation Temperature T_0 (K)*	Total Enthalpy H_0 (MJ/kg)*	Number of Shots
3 km/s - Air	1.89 ± 0.02	9.33 ± 0.07	3229 ± 53	3.79 ± 0.08	22
3 km/s - N_2	1.89 ± 0.02	10.01 ± 0.17	3381 ± 68	3.81 ± 0.09	3
4 km/s - Air	3.13 ± 0.04	10.02 ± 0.22	6079 ± 106	10.37 ± 0.25	8
4 km/s- N_2	3.22 ± 0.04	10.54 ± 0.26	7209 ± 73	10.90 ± 0.24	3

*Estimated from NASA CEA.

The nozzle expansion was simulated using CEA in "rocket" mode where the flow was assumed to be chemically frozen at the nozzle throat. Here CEA was initialized using the measured P_0 and calculated T_0 listed in Table 2. The CEA-calculated freestream parameters including pressure P_∞, temperature T_∞, and velocity U_∞ are listed Table 3. Additionally, these CEA values are compared to nonequilibrium freestream predictions discussed subsequently.

B. N_2 and O_2 CARS

The CARS technique was used to measure rotational and vibrational temperatures of N_2 and O_2 in the freestream of the shock tunnel. Generating adequate signal in the high-temperature, low-density freestream flow required long measurement volumes. A colinear CARS arrangement would have an interaction length longer than the core flow diameter, biasing the measurement from regions outside the core flow. To mitigate this, a nanosecond unstable-resonator spatially enhanced detection (USED) CARS [26]arrangement was used. This yielded a probe volume with 90% of the total CARS signal generated within 50 mm, contained entirely within the core flow. A schematic of the experimental setup is shown in Fig. 1.

The setup used a Spectral Energies "Quasimodo" burst-mode laser, which provided both the 532- and 355-nm, 10-ns pulses at 100 kHz for a burst duration of ~1.2 milliseconds (ms). To generate the broadband Stokes beam for the CARS process, a noncolinear optical parametric oscillator (NOPO) was pumped by the 355-nm output from the burst-mode laser with ~60 mJ/pulse with a conversion efficiency of ≈ 10%. The output wavelength was centered at 580 nm for O_2 CARS and 607 nm for N_2 CARS. The signal-resonant OPO cavity was formed by two flat mirrors composed

of a high reflector for wavelengths λ = 598–610 nm and an output coupler with reflectance *R* = 65% for 598-610 nm and high transmission at λ = 355 nm. An uncoated type-I beta-barium-borate (BBO) crystal was used in the OPO, with a height and width of 10 mm and 12 mm in length. The optical axis of the crystal was cut at 32.8-degrees with respect to the crystal face. The OPO cavity was mounted on a rotary stage allowing the optical axis to be rotated 5 degrees with respect to the 355-nm pump. This effectively matched the group velocities of the signal and idler beams, which allows for broad bandwidth generation [20, 27].

The USED CARS setup utilized the 532-nm from the burst-mode to form the CARS pump beams, and the broadband output from the NOPO was used for the Stokes beam. A 76-mm diameter 532-nm high-reflector with an 11-mm aperture in the center was used to form the annular pump beams. The Stokes beam passed through the 11-mm aperture and both beams were crossed at the nozzle centerline 7 cm downstream of the nozzle exit using a 750-mm lens. Window extensions were used on the side walls of the shock tunnel to avoid generation of CARS signal outside of the tunnel. The pulse energy for the CARS pump beam was 80 mJ and the Stokes pulse was 5 mJ. The CARS signal was separated from the probe beam using several dichroic 473-nm high reflectors and three bandpass filters centered at 470 nm with a 20-nm full width at half maximum (FWHM) cutoff. Additionally, a spatial filter was used to minimize interference from the luminous shock tunnel flow. A 0.75-meter spectrometer (Princeton Instruments SpectraPro HRS-750) with an 1800-lines/mm grating dispersed the CARS signal onto an electron-multiplying (EM)-CCD camera (Princeton Instruments Pro-EM-HS 1024). This EM-CCD enabled fast, 100-kHz acquisition of spectra by vertically shifting charge on each successive laser shot and using the entire 1024 x 1024-pixel chip. The detector used a masked adjacent 1024-pixel square to store all single-shot CARS spectra acquired during the burst prior to sensor readout.

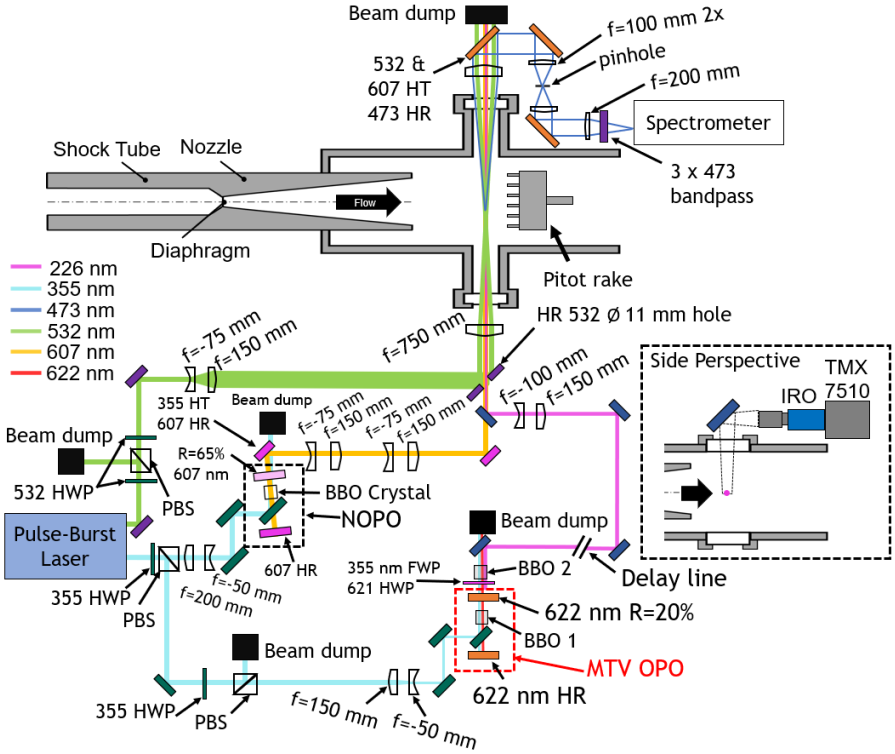

Fig. 1 Burst-mode NO MTV and CARS Schematic with the shock tunnel.

Single-laser-shot CARS spectra were acquired in the shock-tunnel flow at 100 kHz. In post-processing, a three-sample running average was used before fitting the data. This addressed cross talk between adjacent images of the CARS beam on the EM-CCD detector. The spectra were background subtracted and normalized by nonresonant CARS spectra acquired in argon, approximately 15–30 minutes before each shot. The CARS spectra were analyzed using an in-house spectral fitting code implemented in Python. The measurement uncertainty associated with the CARS instrument is taken to be the fit error, which is within typically 4%. At the approximately 300 Pa freestream static pressure encountered, the Doppler linewidth in N_2 was 17–30 times larger than the collision width for rotational/translational temperatures between 200 K and 300 K. All Raman lines were, therefore, modeled using the complex-valued Voigt profile, which is dominated by the Doppler contribution. The CARS susceptibility was convolved with an assumed transform-limited probe pulse and with a detection system response that was a Voigt

profile with ~1 cm^{-1} Gaussian and ~0.5 cm^{-1} Lorentzian widths. This detection system response was determined by fitting CARS spectra acquired in 300 Pa air at room temperature. The nonequilibrium vibrational mode is assumed to be Boltzmann distributed by a vibrational temperature, T_v, with an independent rotational temperature, T_r, used to describe the rotational distribution. CARS spectra from the rotationally cold freestream gases are dominated by the Raman-resonant response, and the nonresonant background was neglected in the fitting routine to accelerate the fitting for rotational and vibrational temperatures. Inclusion of the nonresonant susceptibility as a fitting parameter had a negligible influence on the results. Fitting parameters included T_r, T_v, wavenumber axis shift, and a small vertical offset to the calculated spectrum. Due to the stiff nature of the fitting algorithm, T_r and T_v were fit independently when T_v was low.

Sample fits to a single-laser-shot for N_2 and O_2 CARS spectra are shown in Fig. 2(a-b) for the 3 km/s condition in synthetic air. An N_2 fit for the pure nitrogen 4 km/s case is shown in Fig. 2(c). The 3 km/s spectra exhibit several narrow peaks, corresponding to *Q*-branch transitions from vibrational levels v = 0, 1. A third vibrational peak at v = 2 is observed in the 4 km/s case. Vibrational temperature is indicated by the relative strengths of the vibrational bands. T_v increases as the strength of the v = 1 and 2 bands near 2300 cm^{-1} and 2275 cm^{-1} increases relative to the ground-state peak at ~2330 cm^{-1}. Rotational temperature is reflected in the widths of the vibrational bands, with a narrower *Q*-branch indicating lower T_r. The spectrum in Fig. 2(c) indicates pronounced thermal nonequilibrium where T_v = 2957 K and T_r = 419 K. For comparison, equilibrium expansion of the shock tunnel nozzle flow to T = 419 K would result in a CARS spectrum with only the v = 0 band present. Optical emission from the first negative system of N_2^+ [28] was observed to the right of the v = 0 vibrational band in Fig. 2(c). Optical emission from the freestream was only observed for the 4 km/s pure nitrogen condition and had no effect on the fitting routine.

N_2 temperatures were obtained with synthetic air using eleven and three shots at the 3 km/s and 4 km/s conditions, respectively. Five N_2 shots with ambient air were acquired at the 3 km/s condition. Additionally, N_2 temperatures were obtained with pure nitrogen as the test gas using three shots for both the 3 km/s and 4 km/s conditions. O_2 measurements are more challenging owing to reduced signal levels resulting from lower species concentration. To increase the signal to noise ratio, the O_2 CARS spectra were two-shot averaged on the camera chip, and in post-processing the images were binned down to a 5 kHz repetition rate. O_2 temperatures were measured during three separate experiments at 3 km/s only.

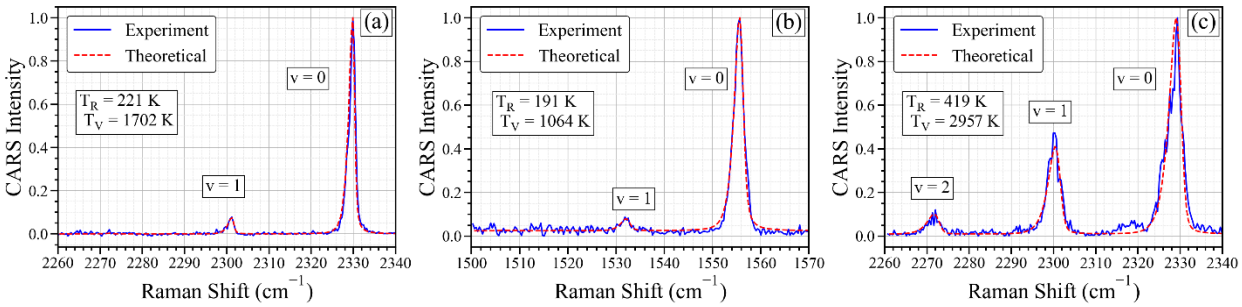

Fig. 2 Sample CARS spectra in synthetic air for the 3 km/s condition for (a) N_2, (b) O_2. (c) Sample CARS spectra in pure N_2 for the 4 km/s condition.

C. NO MTV

The NO MTV setup was operated simultaneously with the CARS system shown in Fig. 1. The OPO was pumped by the 355-nm output from the burst-mode laser by splitting the main 355-nm output using a polarizing beam splitter (PBS). The OPO consisted of a 12-mm long type-I BBO crystal cut at 32.8-degrees and two flat mirrors composed of a high reflector for wavelengths λ = 600-640 and 820-870 nm and an output coupler with R = 20% at both wavelengths. The OPO was pumped with ≈ 80 mJ/pulse of 355-nm, resulting in an output of ≈ 5 mJ/pulse at 622-nm. The 622-nm OPO output and the residual 355-nm pump beam passed through a custom waveplate that aligns the polarizations for sum-frequency generation (SFG) in a second type-I BBO crystal cut at 59.1-degrees. The SFG process generated ≈ 200 μJ/pulse at 226 nm with a bandwidth of ≈ 15 cm^{-1} to excite multiple rotational levels near the (0,0) bandhead of the NO $A^2\Sigma$ - $X^2\Pi$ system. The NO MTV beam passed through the aperture in the 532-nm high reflector of the USED CARS set-up to generate NO LIF signal colinear with the CARS measurement. An uncoated 750-mm lens focused the beams to a waist region near the spanwise centerline of the test section, generating LIF emission that was captured using a UV-sensitive image intensifier (LaVision HS-IRO S20) coupled to a high-speed Phantom TMX 7510 monochrome camera mounted on top of the shock tunnel test section.

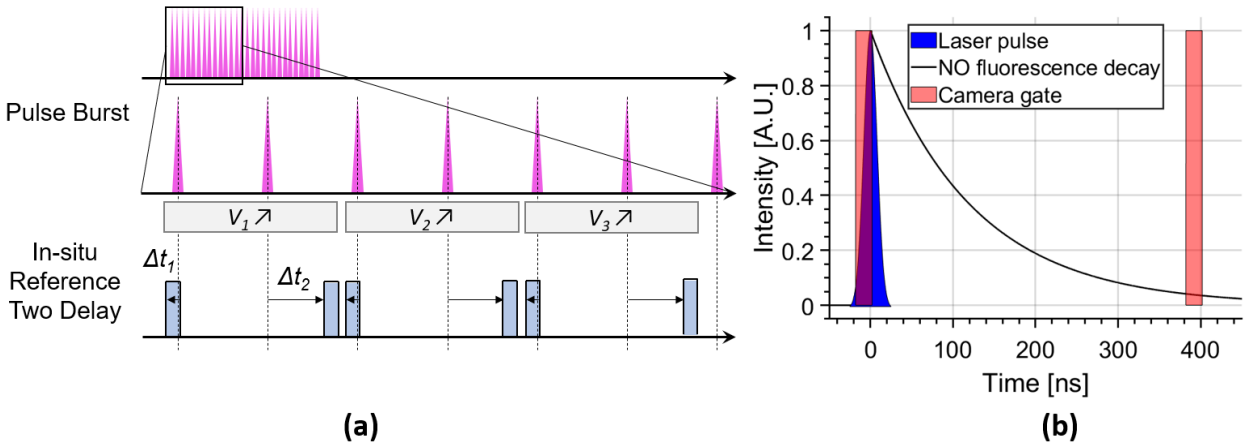

Fig. 3. (a) Timing schematic for NO MTV diagnostic. Laser pulses denoted in purple; intensifier gates shown in blue. (b) Zoom-in showing the camera gate with respect to the NO fluorescence decay.

The MTV diagnostic used a two-image in-situ reference approach for velocimetry measurements as shown Fig. 3(a). This approach used a reference image at t_0 and a displacement image at a time delay Δt after the reference image. Due to the limited intensifier speed of the IRO, it was not possible to image the same fluorescence from a single pulse using two intensifier gates. Instead, a single velocity measurement was taken using two sequential laser pulses yielding an effective repetition rate of 50 kHz. To avoid dynamic range issues, the intensifier gate for the reference image only overlapped for the first few ns of laser pulse passing through the test section, as shown in Fig. 3(b). The second pulse was taken with a delay time of Δt = 400 ns. The intensifier gate was set to 20 ns for both images. This arrangement allowed for comparable signal-to-noise ratio for the reference and delayed image. The total burst contained ~100 pulses, yielding 50 velocity measurements over the 1-ms burst duration. The images for each cycle were processed using a Voigt fitting routine to estimate the line center position, and a linear regression was fit to the positions. Raw single-shot delay and reference NO MTV images taken during a 4 km/s air case are shown in Fig. 4(a-b). Comparison of the fitted Voigt lineshape to the binned single-shot reference and delay NO MTV images shown in Fig. 4(c) display excellent agreement. The measurement uncertainty associated with the NO MTV instrument is taken to be the fit error, which is within typically 1%. MTV data were obtained on 10 shots for the 3 km/s – air condition and 5 shots for the 4 km/s – air condition.

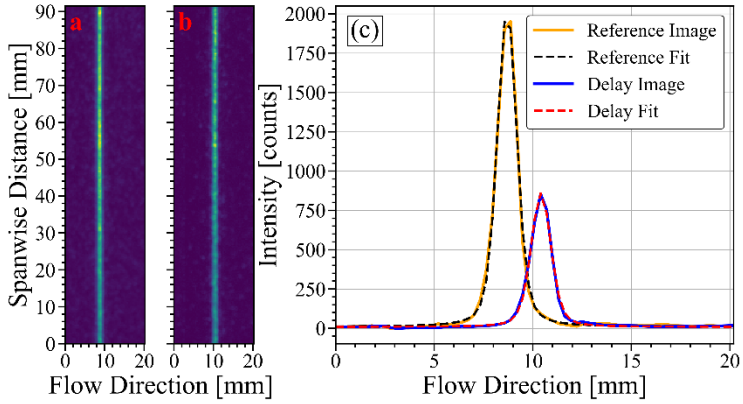

Fig. 4. Single-shot NO MTV images taken during a 4 km/s air case for (a) reference and (b) delay. (c) Comparison of binned reference and delay NO MTV data to the fitted lineshape.

D. NO LAS

The LAS diagnostic used two quantum cascade lasers to measure rotational and vibrational temperatures and the partial pressure of NO at 25 or 100 kHz. The beams were both fiber coupled into one single-mode fiber. The collimated, colinear beams were pitched through the test section where 3D printed flow cutters were used to isolate the quasi-uniform core flow. The beams were positioned 2 cm from the nozzle exit and the absorbing path length was

23.2 cm. The measurement uncertainty associated with the LAS instrument is taken to be the fit error, which is within typically 2.5%. Further details on the LAS diagnostic can be found in Gilvey et al [22].

III. Freestream Nonequilibrium Modeling

The SPARC computational fluid dynamics (CFD) code was used for flow simulation of the shock tunnel. SPARC is a finite-volume compressible CFD code which solves the Reynolds-Averaged Navier–Stokes (RANS) equations. SPARC has a variety of gas chemistry models available; herein, SPARC used a 5-species air chemistry mechanism (N_2, O_2, N, O, and NO) [29] and a species-specific, multi-vibrational temperature model [30]. The multi-vibrational temperature model treats each diatomic species separately and accounts for vibrational energy transfer between species [9]. To determine the species concentrations and translational, rotational, and vibrational temperatures, a finite-rate chemistry model assuming thermally perfect gas was used [31]. Additionally, a two-temperature model [29] assuming a single vibrational temperature among all diatomic species is also used for comparison. Additional details on the relaxation rates used in SPARC can be found in Appendix A.

The simulations used an axisymmetric, combined grid for the stagnation region, nozzle, and test section. The stagnation conditions were set to the mean values of Table 2, and NASA CEA was used in "rocket" mode to initialize the flow quantities in the contraction and expansion regions of the nozzle. This approach allowed the nozzle flow to converge within 10,000 solver iterations, corresponding to 3 ms of actual flow time.

Simulation results along the nozzle centerline for the different flow conditions are shown in Fig. 5. Additionally, the nozzle exit (freestream) values are summarized in Table 3 and compared to CEA. Consider first the air cases in Fig. 5 (top row). For both conditions, the rotational temperature is similar between the multi-temperature and two-temperature models. However, large discrepancies are observed in the vibrational temperatures, particularly for nitrogen. Between the conditions, the vibrational nonequilibrium is observed to be greater for the 4 km/s condition, with a nitrogen vibrational temperature of 2066 K compared to 1807 K for the 3 km/s condition. Next, consider the nitrogen cases, where there is only a single vibrational temperature. The 3 km/s condition achieves a vibrational temperature of 2561 K, and the 4 km/s condition reaches 3740 K. This indicates that there are fewer equilibration reactions occurring in the nitrogen cases due to the fewer species present throughout the expansion. As a result, the final predicted vibrational temperature reflects the higher temperature in the stagnation region prior to expansion. Finally, at 3 km/s, good agreement between temperature (T_∞ and T_r), P_∞, and velocity is observed when comparing the CEA and SPARC predictions, whereas larger discrepancies exist in the 4 km/s case.

Table 3: Summary of Calculated HST Freestream Conditions using SPARC and CEA

Condition	CEA P_∞ (Pa)	SPARC P_∞ (Pa)	CEA U_∞ (km/s)	SPARC U_∞ (km/s)	SPARC P_{PITOT} (kPa)	*CEA* T_∞ [K]	*SPARC* T_r [K]	N_2 T_v [K]	O_2 T_v [K]	NO T_v [K]
3 km/s – air	182 ± 1	187	2.73 ± 0.02	2.67	19.0	204 ± 5	183	1807	1109	394
4 km/s – air	159 ± 2	267	3.93 ± 0.04	4.17	21.2	315 ± 2	551	2066	888	708
3 km/s – N_2	183 ± 1	179	2.79 ± 0.03	2.67	20.0	205 ± 6	161	2561	-	-
4 km/s – N_2	229 ± 1	230	4.34 ± 0.03	4.36	22.1	556 ± 1	496	3740	-	-

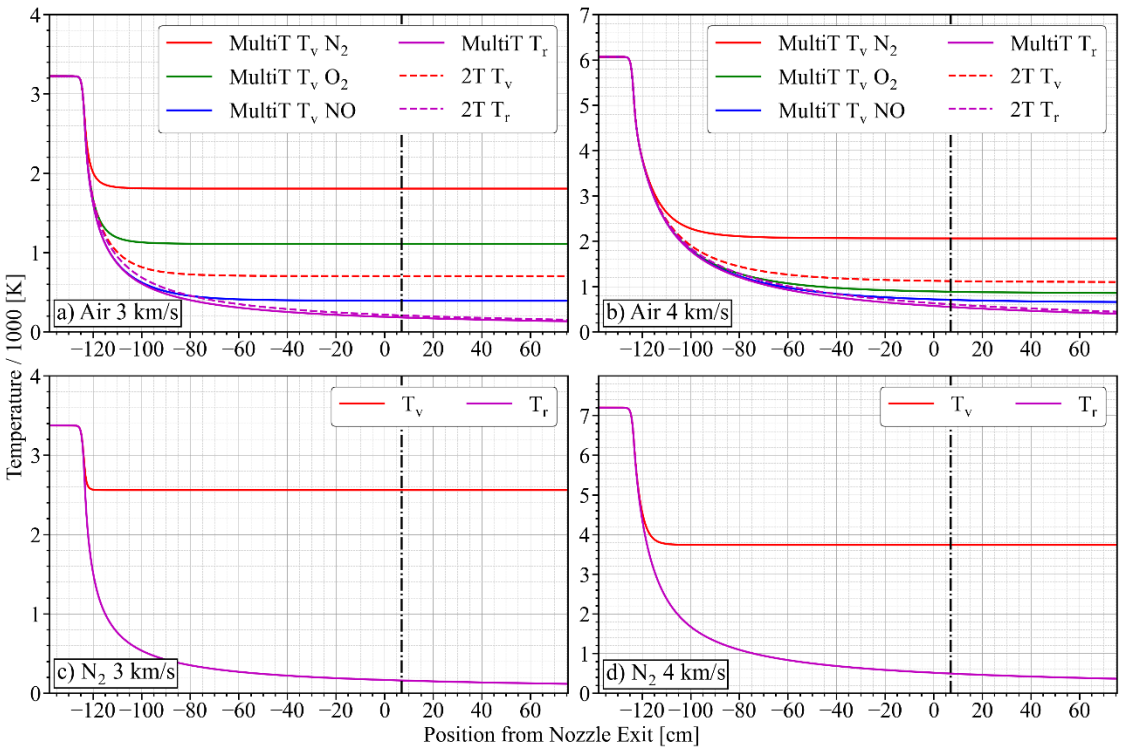

Fig. 5. Simulation results along the centerline of the nozzle. Solid lines represent multi-vibrational ("MultiT") temperature results, dashed lines two-temperature ("2T") results. Vertical dashed line indicates CARS/MTV measurement location.

IV. Results

A. 3 km/s – Synthetic Air Condition

Ensemble-averaged temporal profiles of stagnation pressure, Pitot pressure, freestream temperatures, and freestream velocity are shown in Fig. 6 at the 3 km/s – air test condition. The time-varying uncertainty shown in Fig. 6 is the root-sum-squared value of the shock tunnel shot-to-shot precision uncertainty and the fitting routing uncertainty described previously. The precision uncertainty here is the standard error, which is the standard deviation divided by the square root of the number of runs, across all the runs for each time instance. The fitting routine uncertainty is the fit error standard deviation averaged across all the runs at each time. These measurements are averaged over the defined test time and summarized in Table 4 where the uncertainties of the mean correspond to the time-average of the total uncertainty during the quasi-steady test time. The velocimetry is an ensemble average of 10 runs while the pressure is an ensemble average of 22 runs at this condition. The stagnation pressure, P_0, trace (top row) exhibits a sharp pressure rise following the passage of the incident shock defined here to be $t = 0$ µs. The pressure then increases in multiple steps from 110 µs < t < 250 µs owing to shock bifurcation associated with separation of the incoming boundary layer [32]. The overshoot of the stagnation pressure is related to both shock bifurcation and continuing compression of the driver gas by the piston following diaphragm rupture [21]. As annotated in Fig. 6, a region of quasi-steady stagnation pressure and test time is defined to follow. This ≈ 660-µs region begins after the initial pressure transients and ends when the stagnation pressure has decreased by 20%. The start of this quasi-steady test time was determined by using a cross-correlation between the stagnation and pitot pressures to find the time of flight delay and the start of the quasi-steady test time of the pitot pressure was subtracted by this time of flight to yield the initial start time. The measured P_0, as shown with the dashed line and listed in Table 2, is taken as the average over this time window and is used to initialize nozzle simulations with SPARC and CEA. The Pitot pressure, P_{Pitot}, shown in the second row exhibits a similar complex shape like the stagnation pressure. Once more, the quasi-steady test time is defined to begin following initial transients, which in this case occurs at the local minimum annotated in the figure. The test time length is 660-µs, which occurs while the Pitot pressure resides within ≈ ±10% of the average

value listed in Table 4. Unlike the P_0, however, which monotonically decreases, the Pitot pressure first increases and then decreases during the defined test time.

The freestream velocity versus time is shown in Fig. 6 (third row). Initially, U_∞ is about 3.2 km/s per second shortly after the arrival of the starting shock at ≈ 400 μs. The velocity then decays by ≈ 20% to a constant value of approximately 2.7 km/s over the quasi-steady test time. This decrease in freestream velocity occurs while the Pitot pressure increases. Here, and for all laser measurements in Fig. 6, the quasi-steady test time is shifted earlier by 61 μs, which corresponds to the time of flight between the Pitot and laser diagnostics measurement locations at the freestream velocity. The freestream velocity measurements are in good agreement with the CEA and SPARC models (Table 3). Freestream velocity measurements in the T5 reflected shock tunnel [15] were also in good agreement with nozzle code predictions.

CARS-measured time histories of the freestream N_2 and O_2 rotational and vibrational temperatures are shown in Fig. 6 (fourth and fifth rows). The figures also include comparisons to NO T_r and T_v from LAS as further described in [22]. Eleven, three, and six experiments were averaged for the N_2, O_2, and NO plots, respectively. As the tunnel flow starts, the rotational temperatures increase while the freestream velocity decreases. This trend could be expected as energy is transferred from kinetic to internal energy as the flow deaccelerates. Following the initial transient, the measured NO, O_2, and N_2 rotational temperatures agree to within the uncertainties. The NO, N_2, and O_2 rotational temperatures are within approximately 10% of the SPARC prediction over most of the quasi-steady test time. The rotational temperature of each species should rapidly relax to a common value. Given this, and the relatively low scatter in the LAS data, the NO T_r is defined as the bulk gas rotational temperature in Table 4.

The vibrational temperatures display less of an initial transient than the rotational temperatures and freestream velocity. The O_2 T_v of about 934 K is about 15% less than the SPARC prediction. The N_2 vibrational temperature during the quasi-steady test time is approximately 1624 K, which is about is 10% lower than that predicted in the simulation. In contrast, the vibrational relaxation of NO is slower than predicted by SPARC with the NO T_v temperature of ≈ 770 K being about two times greater than the prediction.

In summary, pronounced thermal nonequilibrium is observed between the rotational and vibrational temperature of all three species at the 3 km/s condition. The SPARC model accurately predicts the rotational temperature and the freestream velocity. Vibrational relaxation is fastest for NO and slowest for N_2, an observation consistent with the multi-vibrational SPARC predictions. The current multi-vibrational temperature model captures this trend, but underpredicts NO T_v while overpredicting N_2 and O_2 T_v.

Table 4: Summary of HST Freestream Measurements

Condition	P_{PITOT} [kPa]	Test Time (ms)	U_∞ (km/s)	T_r [K]	N_2 T_v [K]	O_2 T_v [K]	NO T_v [K]
3 km/s – air	21.8 ± 0.2	0.7	2.7 ± 0.04	195 ± 2	1624 ± 53	934 ± 37	772 ± 19
4 km/s – air	29.1 ± 0.5	0.5	4.2 ± 0.04	543 ± 17	1693 ± 160	-	574 ± 39
3 km/s – N_2	22.1 ± 0.5	0.6	-	184 ± 44	1959 ± 200	-	-
4 km/s – N_2	30.1 ± 0.8	0.5	-	469 ± 57	2494 ± 350	-	-

B. 4 km/s – Synthetic Air Condition

Ensemble-averaged freestream values are presented in Fig. 7 at the 4 km/s test condition. The figure layout and measured parameters are identical to Fig. 6 with the exception that O_2 temperatures were not measured at the 4 km/s condition and the quasi-steady test time is shifted earlier by 41 μs corresponding to the time of flight between the Pitot and laser diagnostics measurement locations at the freestream velocity. The mean values and uncertainties over the test time are summarized in Table 4. The pressure measurements used 10 runs and the velocimetry used 5 runs at this condition. Like the 3 km/s case, a region of quasi-steady stagnation pressure follows the initial transients associated with reflected shock bifurcation and pressure overshoot. During this time, the stagnation pressure decreases by about 20%. In this case, the quasi-steady test time as measured in the stagnation chamber is approximately 640 μs. The Pitot pressure (row 2) shape once again shows similarity to the stagnation pressure and the quasi-steady test time begins following initial transients. The test time length is defined to be ~460 μs, which occurs while the Pitot pressure resides within ≈ ± 10% of the average value listed in Table 4. The Pitot pressure increases and decreases during the test time just as the 3 km/s case.

Like the 3 km/s case, the freestream velocity in Fig. 7 initially decreases while the rotational temperature increases. During the quasi-steady test time, the N_2 and NO T_r agree to within the uncertainty. The average NO T_r during the test time (Table 4) is within 10% of the SPARC prediction. The average freestream velocity of 4.17 km/s is in agreement with the SPARC model, but 5% higher than CEA. The rotational temperature decreases over the quasi-

steady test time, while the freestream velocity increases. In T5 simulations, Gross and Schwartzentruber [17] note that helium from potential driver gas contamination would produce a similar behavior.

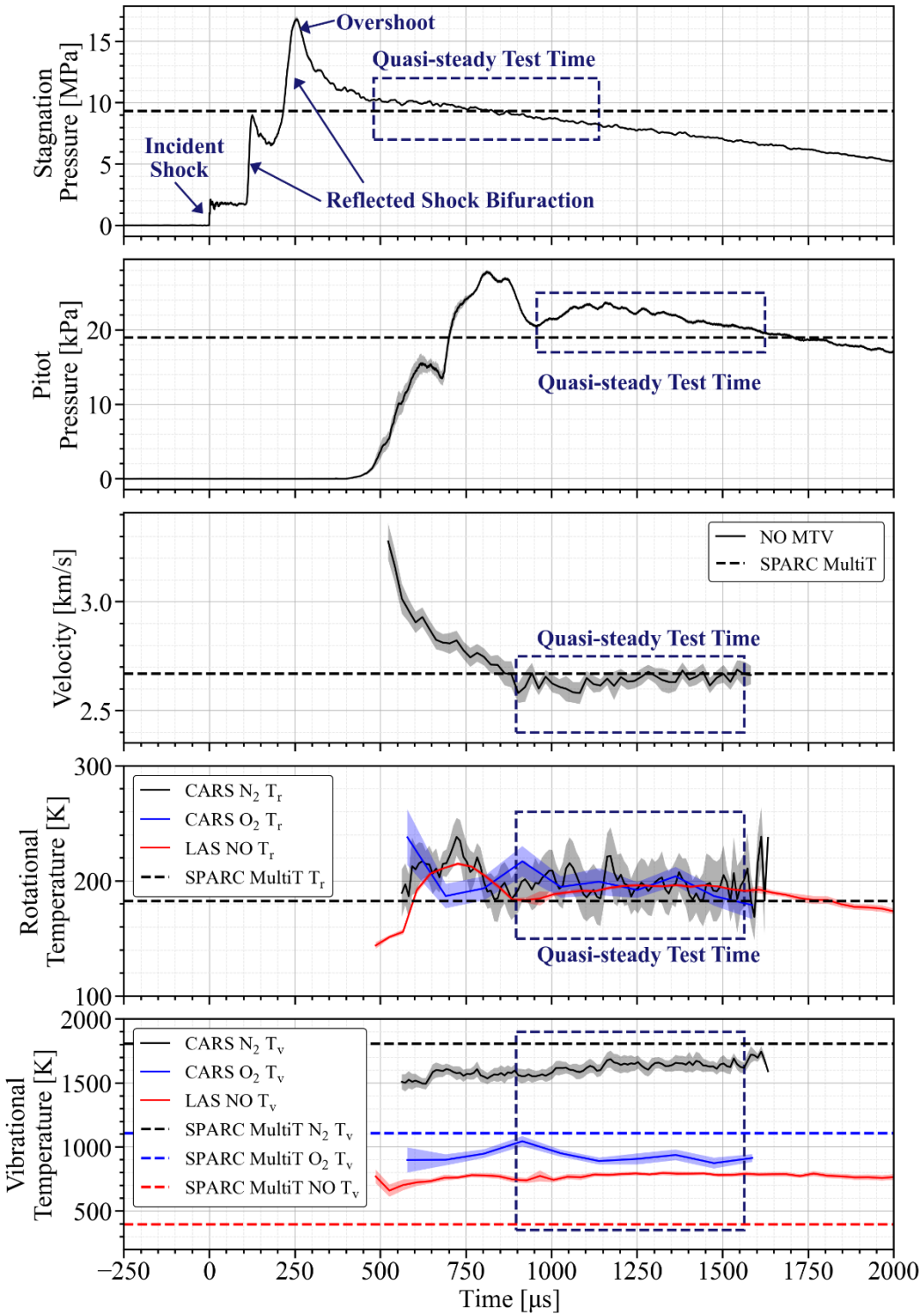

Fig. 6. Time-synchronized plot of ensemble-averaged pressures, velocity, and temperatures for the 3 km/s condition. Shading indicates uncertainty on the mean. Dashed horizontal lines indicate SPARC predictions.

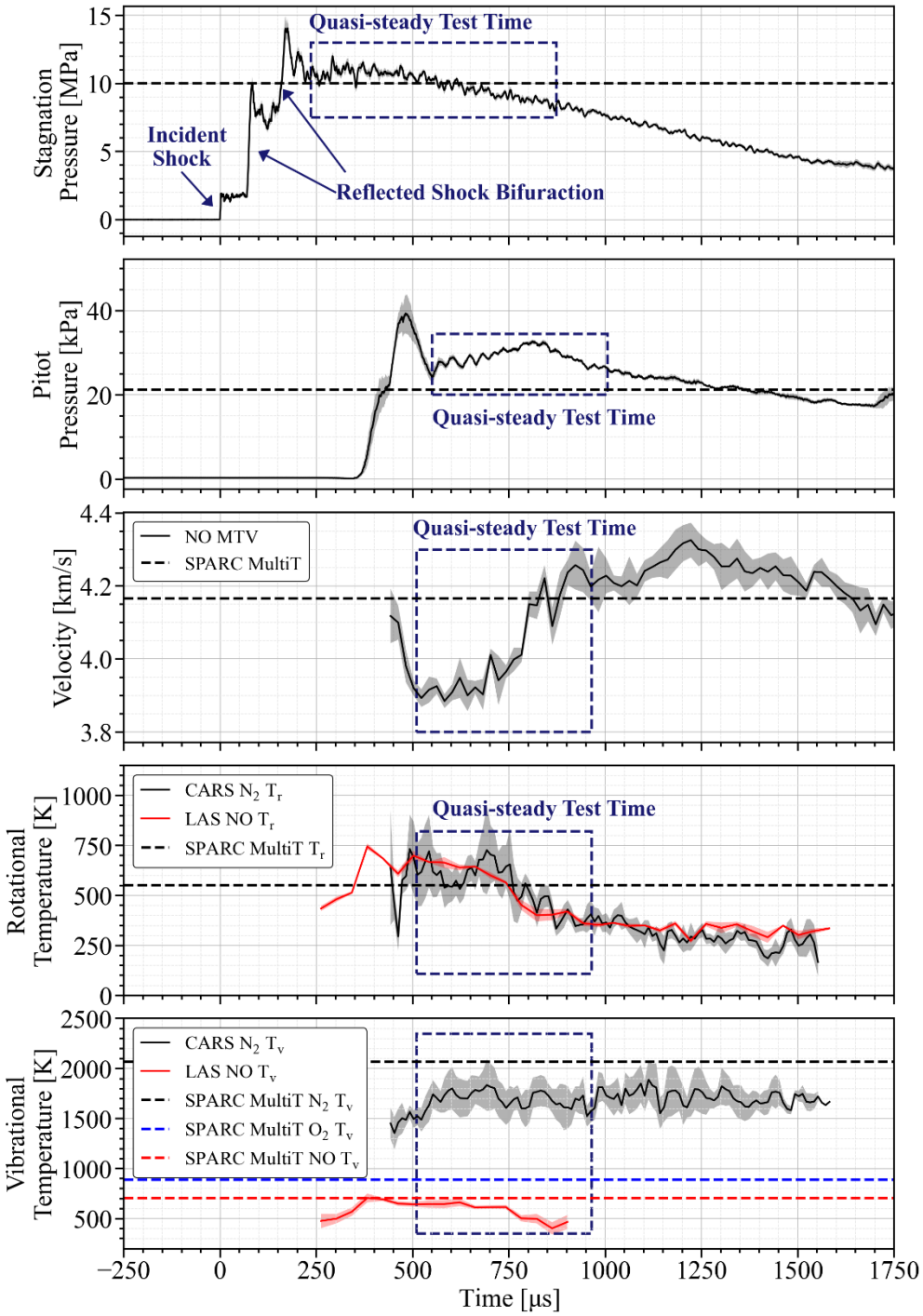

Fig. 7. Time-synchronized plot of ensemble-averaged pressures, velocity, and temperatures for the 4 km/s condition. Shading indicates uncertainty on the mean. Dashed horizontal lines indicate SPARC predictions.

The SPARC vibrational temperatures are in better agreement with the 4 km/s data than the 3 km/s. The N_2 vibrational temperature is measured to be ≈ 10% lower than the prediction, whereas NO T_v measurement is ≈ 20% lower than SPARC. In contrast to the 3 km/s case, the modeled relaxation of NO is slower than the experiment.

C. 3 km/s – Ambient Air Condition

To understand the effect that water vapor has on nonequilibrium state of the nitrogen in the flow, ambient air from the laboratory was used as the test gas. A handheld hygrometer (General Tools EP8709) was used to measure the relative humidity of the air for each shot. Five shots with humid air at the 3 km/s condition were performed with a water mole fraction of 0.0036 ± 0.0004 (3600 PPM). A comparison of the freestream N_2 temperatures with synthetic air is shown against the ensemble-averaged freestream measurements with humid air in Fig. 8. The addition of water vapor to the test gas has no discernable effect on the nonequilibrium state of N_2 in test section within the measurement scatter. Humid air measurements were also performed in Gilvey et al [22] with a water mole fraction of ~0.009 (~9000 PPM) in the test gas. Similar to the N_2 CARS measurements shown in Fig. 8, the measured NO rotational and vibrational temperatures were unchanged in the freestream of the shock tunnel with the added water content to the test gas. Laser absorption measurements of the water content in the freestream showed that any water dissociation in the plenum had recombined by the time the gas reached the test section. Direct addition of humid air as the test gas differs from the water contamination measurements in the T5 facility [15], which postulated that the water contamination originated from the internal surfaces of T5.

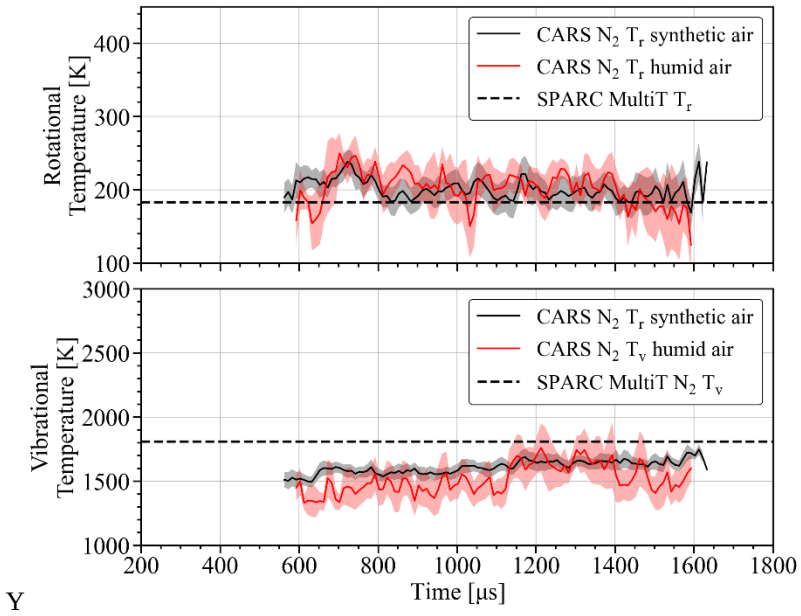

Fig. 8. Comparison of ensemble-averaged N_2 CARS rotational and vibrational temperature for synthetic air and humid air for the 3 km/s condition. Shading indicates on the mean. Dashed horizontal lines indicate SPARC predictions.

D. 3 and 4 km/s – Pure N_2 Condition

To remove the effect of oxygen chemistry on the gas relaxation during the nozzle expansion, pure nitrogen replaced the synthetic air as the test gas for three shots for both the 3 and 4 km/s condition. Comparisons of the ensemble-averaged temporal profiles of the freestream temperatures are shown in Fig. 9 for pure nitrogen test gas at the 3 km/s and 4 km/s condition. The quasi-steady test time based on Pitot pressure data is annotated in the figure for each condition. The 3 km/s rotational temperature is nearly constant and in good agreement with the SPARC prediction. Like the 4 km/s – air condition, the pure N_2 case displays a decrease in rotational temperature over the quasi-steady test time duration and is in good agreement with SPARC prediction in the early half of the quasi-steady test time. Like the air cases, the mean vibrational temperatures at both conditions are lower than the SPARC model, indicating that the modeled relaxation of N_2 is slower than the experiment.

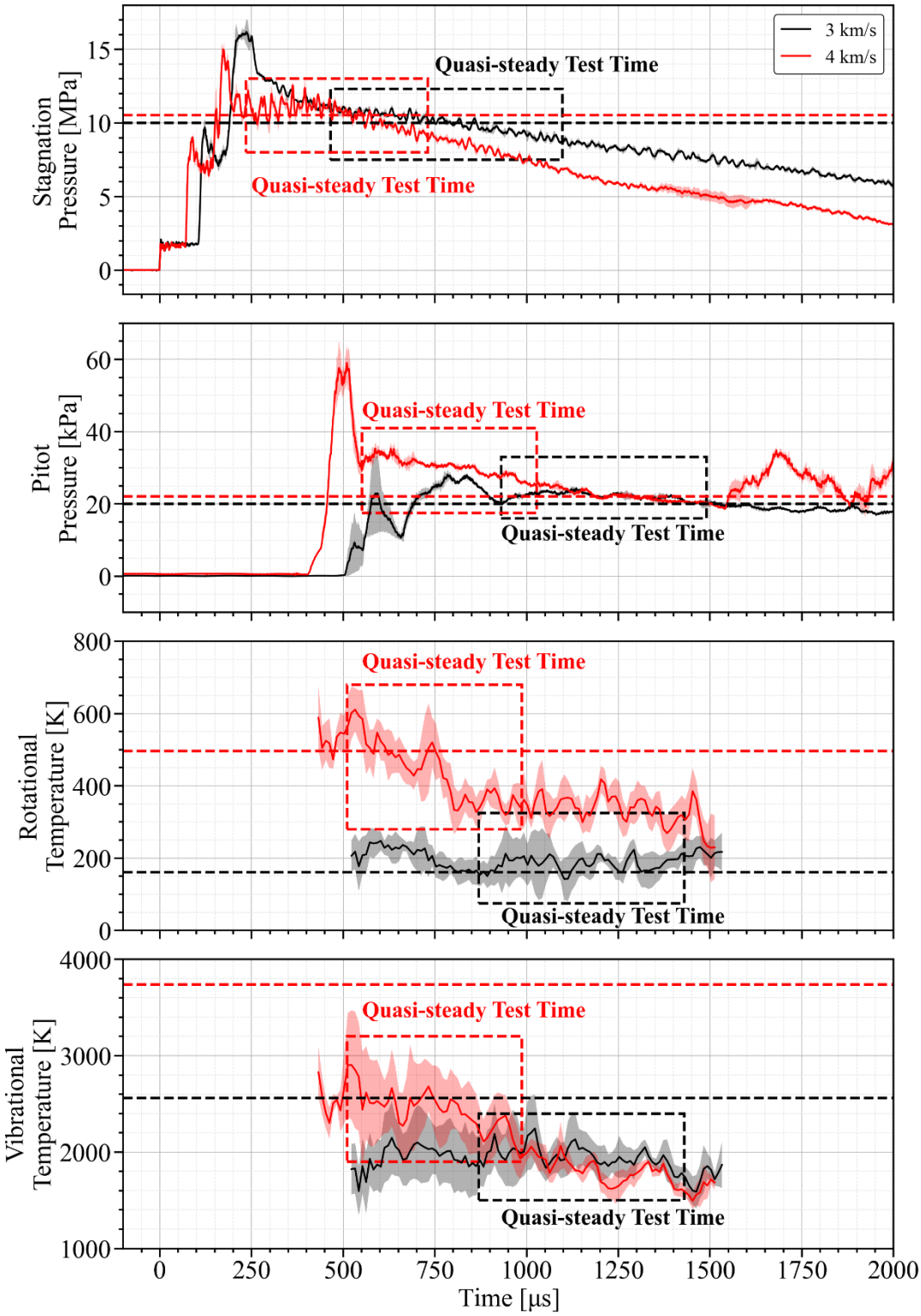

Fig. 9. Time-synchronized plot of ensemble-averaged pressures, velocity, and temperatures for the 3 km/s and 4 km/s conditions in pure N_2. Shading indicates uncertainty on the mean. Dashed horizontal lines indicate SPARC predictions.

Conclusions

A novel combination of high-speed laser spectroscopy measurements for freestream velocimetry and multi-species internal temperatures has been performed over an extensive number of repeat experiments in Sandia's reflected shock tunnel. The resulting dataset allowed for meaningful trends between experimental conditions and molecular temperatures to be discovered. Additionally, the combined dataset served as a benchmark for comparison to nonequilibrium freestream modeling using the SPARC CFD code.

Experiments were performed in synthetic air at two flow conditions corresponding to 3 and 4 km/s nominal freestream velocities at stagnation temperatures of ≈ 3200 K and 6100 K, respectively. The measurements were able to resolve starting transients where the freestream velocity decreased while the rotational temperature increased before reaching approximately constant values over a defined quasi-steady test time based on concurrent Pitot pressure measurements.

At the 3 km/s – air condition, significant nonequilibrium was measured between the rotational and vibrational temperatures with T_r residing near 200 K and vibrational temperatures for N_2, O_2, and NO well above T_r. The highest vibrational temperature was N_2 at 1624 K. O_2 and NO were lower and closer together at 934 and 772 K, respectively. Comparison with CFD modeling showed good agreement with the measured velocity during the quasi-steady test time and between measured rotational temperatures. Vibrational temperatures of N_2 and O_2 were overpredicted, whereas vibrational temperatures of NO were underpredicted.

For the 4 km/s – air condition, a stable test time of nearly 0.5 ms was observed, but larger transients were seen after the test time was over. During the run time of the tunnel, the velocity showed a gradual increase from 3.8 km/s to 4.3 km/s at the end of the test time. This decrease in freestream velocity corresponded with a gradual decay in rotational temperature. The predicted vibrational temperatures for N_2 and NO were in closer agreement to experimental values than the 3 km/s condition.

To isolate oxygen chemistry effects on the N_2 thermal relaxation during the flow expansion, pure nitrogen was also used as a test gas. With the lack of other collisional partners, the pure N_2 condition showed elevated vibrational temperatures for both the 3 and 4 km/s conditions. Comparison of the experimental data with the CFD predictions showed good agreement with the rotational temperatures. The measured N_2 vibrational temperatures were lower than the CFD predictions at both conditions, consistent with the air cases.

An additional configuration was run using humid air to test the effect water has on N_2 nonequilibrium at the 3 km/s condition. With 3600 ppm of water present, both the rotational and vibrational temperatures of N_2 were nearly identical to the previous 3 km/s synthetic air cases showing little dependence on water at these levels.

Acknowledgements

The authors would like to acknowledge Dr. Brad Maeng for his assistance in maintaining the multi-vibrational temperature model in SPARC.

Sandia National Laboratories is a multi-mission laboratory managed and operated by National Technology & Engineering Solutions of Sandia, LLC, a wholly owned subsidiary of Honeywell International Inc., for the U.S. Department of Energy's National Nuclear Security Administration under contract DE-NA0003525. This paper describes objective technical results and analysis. Any subjective views or opinions that might be expressed in the paper do not necessarily represent the views of the U.S. Department of Energy or the United States Government.

Appendix A. SPARC Relaxation Rates

Details of the relaxation rates used in SPARC to model the species-specific vibrational temperatures are discussed in this appendix. The species-specific, multi-temperature model relies on vibrational-translational (V-T) and vibrational-vibrational (V-V) relaxation rates obtained from literature. The V-T rates follow the expression from Millikan and White [33] with units of atm·seconds.

$$P_s\tau = \exp\left(a\left[T^{-\frac{1}{3}} - b\right] - 18.42\right) \quad \text{A1}$$

The V-T relaxation rates used in SPARC for the CFD predictions are provided in Table A1.

For V-V relaxation, an empirical expression modified from Kim et al [34] is used

$$P_s\tau = AT^B + CT^D + E \quad \text{A2}$$

where the relaxation rate is in units of Pa·seconds. The V-V coefficients used in SPARC are provided in Table A2. For predictions presented in this paper, only V-T rates from Park [35] and V-V rates from Kim et al and were used. SPARC predictions in Gilvey et al. [22] showed comparisons with the new rates from Streicher [36] replacing the

rates from Park and Kim et al. To verify the accuracy of the coefficients for Eq. A2, V-V relaxation rates were computed theoretically using Eq. A3 from Taylor et al [37]

$$\tau = \frac{1}{P(AB) \cdot Z_{AB}} \tag{A3}$$

where *P(AB)* is the probability per collision of vibrational energy transfer between molecule A and molecule and Z_{AB} is the collision frequency between molecule A and B. An empirical form of *P(AB)* is given by Lee et al [38]. The collisional frequency, Z_{AB}, is taken from Ref. [37]

$$Z_{AB} = \left(\frac{8\pi k_B T}{\mu_{AB}}\right)^{\frac{1}{2}} d_{AB}^2 n \tag{A3}$$

where k_B is the Boltzmann constant, T is temperature, μ_{AB} is the reduced mass given by $m_a \cdot m_b/(m_a+m_b)$, d_{AB} is the average collision diameter given by $(d_A + d_B)/2$ where d_A and d_B are the collision diameters for molecule A and B, and n is number density. Replacing number density with partial pressure allows for comparison to rates provided by Ref. [34]. Comparison of relaxation times calculated from theory are compared to Ref. [34] and Ref. [36] in Fig. A1. It should be noted that the A coefficient for N_2-O_2 V-V relaxation from Kim et al was determined to be incorrect and was off by 3 orders of magnitude.

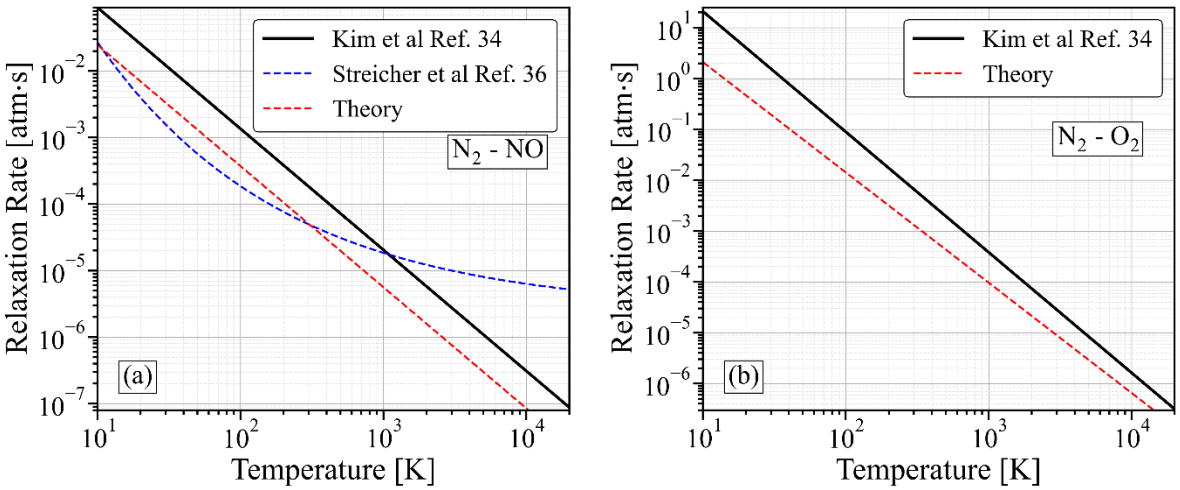

Fig. A1: (a) Comparison of V-V relaxation rate for N_2-NO for Refs. [34, 36] to theory and (b) comparison of V-V relaxation rate for N_2-O_2 for Refs. [34] to theory.

Table A1: Coefficients for V-T relaxation rates used in SPARC

Vibrator	Collider	a	b	Source
N_2	O_2	229	0.0295	[35]
N_2	N_2	221	0.0290	[35]
N_2	NO	225	0.0293	[35]
N_2	O	72.4	0.0150	[35]
N_2	N	180	0.0262	[35]
O_2	O_2	138	0.0300	[35]
O_2	N_2	134	0.0295	[35]
O_2	NO	136	0.0298	[35]
O_2	O	47.7	0.0590	[35]
O_2	N	72.4	0.0150	[35]
NO	O_2	49.5	0.0420	[35]
NO	N_2	49.5	0.0420	[35]
		130	0.0214	[36]
NO	NO	49.5	0.0420	[35]
		70	0.0315	[36]
NO	O	49.5	0.0420	[35]

NO	N	49.5	0.0420	[35]

Table A2: Coefficients for V-V relaxation rates used in SPARC

Vibrator	Collider	a	b	c	d	e	Source
N_2	O_2	3.158×10^{7}	-2.17	0	0	1.31×10^{-10}	Eq. A2
		4.979×10^{8}	-2.37	0	0	1.50×10^{-10}	[34][i]
N_2	NO	1.644×10^{5}	-1.82	0	0	1.17×10^{-11}	Eq. A2
		1.644×10^{5}	-1.82	0	0	2.23×10^{-11}	[34]
		2.750×10^{5}	-2.21	2.568×10^{2}	-0.75	3.81×10^{-1}	[36]
O_2	NO	6.191×10^{5}	-1.82	0	0	1.50×10^{-10}	[34]

[i] A coefficient changed from 4.979×10^{5} given in Ref. 30 to 4.979×10^{8}.

References

1. Gu, S., and Olivier, H. "Capabilities and limitations of existing hypersonic facilities," *Progress in Aerospace Sciences* Vol. 113, 2020, p. 100607.
https://doi.org/10.1016/j.paerosci.2020.100607

2. Fujii, K., and Hornung, H. G. "Experimental investigation of high-enthalpy effects on attachment-line boundary-layer transition," *AIAA journal* Vol. 41, No. 7, 2003, pp. 1282-1291.
https://doi.org/10.2514/2.2096

3. Zander, F., Morgan, R., Sheikh, U., Buttsworth, D., and Teakle, P. "Hot-wall reentry testing in hypersonic impulse facilities," *AIAA journal* Vol. 51, No. 2, 2013, pp. 476-484.
https://doi.org/10.2514/1.J051867

4. Hargis, J. W., Mussoni, E. E., Swain, W. E., Lynch, K. P., and Wagner, J. L. "Carbon-Monoxide Laser Absorption Spectroscopy Measurements over Ablating Graphite in a Shock Tunnel," *AIAA Journal*, 2024, pp. 1-11.
https://doi.org/10.2514/1.J064154

5. Davis, J.-P., and Sturtevant, B. "Separation length in high-enthalpy shock/boundary-layer interaction," *Physics of Fluids* Vol. 12, No. 10, 2000, pp. 2661-2687.
https://doi.org/10.1063/1.1289553

6. Holloway, M. E., Chaudhry, R. S., and Boyd, I. D. "Assessment of hypersonic double-cone experiments for validation of thermochemistry models," *Journal of Spacecraft and Rockets* Vol. 59, No. 2, 2022, pp. 389-400.
https://doi.org/10.2514/1.A35052

7. Nompelis, I., Candler, G. V., and Holden, M. S. "Effect of vibrational nonequilibrium on hypersonic double-cone experiments," *AIAA journal* Vol. 41, No. 11, 2003, pp. 2162-2169.
https://doi.org/10.2514/2.6834

8. Candler, G. V. "Rate effects in hypersonic flows," *Annual Review of Fluid Mechanics* Vol. 51, 2019, pp. 379-402.
https://doi.org/10.1146/annurev-fluid-010518-040258

9. Candler, G. V., and MacCormack, R. W. "Computation of weakly ionized hypersonic flows in thermochemical nonequilibrium," *Journal of Thermophysics and heat transfer* Vol. 5, No. 3, 1991, pp. 266-273.
https://doi.org/10.2514/3.260

10. Palma, P. C., Danehy, P. M., and Houwing, A. "Fluorescence imaging of rotational and vibrational temperature in shock-tunnel nozzle flow," *AIAA journal* Vol. 41, No. 9, 2003, pp. 1722-1732.
https://doi.org/10.2514/2.7290

11. Danehy, P. M., O'Byrne, S., Frank, A., Houwing, P., Fox, J. S., and Smith, D. R. "Flow-tagging velocimetry for hypersonic flows using fluorescence of nitric oxide," *AIAA journal* Vol. 41, No. 2, 2003, pp. 263-271.
https://doi.org/10.2514/2.1939

12. Fraval, E., Danehy, P., and Houwing, A. "Single-shot broadband coherent anti-Stokes Raman scattering measurements in a free piston shock tunnel nozzle expansion," *Proceedings of 23rd International Symposium on Shock Waves*. Citeseer, 2001, pp. 22-27.

13. Parker, R., Wakeman, T., Holden, M., and MacLean, M. "Measuring nitric oxide freestream concentration using quantum cascade lasers at CUBRC," *44th AIAA Aerospace Sciences Meeting and Exhibit*. 2006, p. 926.
https://doi.org/10.2514/6.2006-926

14. Parker, R., Wakeman, T., MacLean, M., and Holden, M. "Measuring nitric oxide freestream velocity using quantum cascade lasers at CUBRC," *45th AIAA Aerospace Sciences Meeting and Exhibit*. 2007, p. 1329.
https://doi.org/10.2514/6.2007-1329

15. Finch, P. M., Girard, J. J., Schwartz, T., Strand, C. L., Hanson, R. K., Yu, W. M., Austin, J. M., and Hornung, H. G. "Measurements of T5 shock tunnel freestream temperature, velocity, and composition," *AIAA Journal* Vol. 61, No. 4, 2023, pp. 1555-1578.
https://doi.org/10.2514/1.J062383

16. Center, R., and Newton, J. "Vibrational Relaxation of N2 by H2O," *The Journal of Chemical Physics* Vol. 68, No. 8, 1978, pp. 3327-3333.
https://doi.org/10.1063/1.436237

17. Gross, T., and Schwartzentruber, T. E. "Freestream Characterization of Hypersonic Wind Tunnels by Combining Measurements and Simulation," *AIAA SCITECH 2023 Forum*. 2023, p. 2090.
https://doi.org/10.2514/6.2023-2090

18. Stalker, R., and Crane, K. "Driver gas contamination in a high-enthalpy reflected shock tunnel," *AIAA Journal* Vol. 16, No. 3, 1978, pp. 277-279.
https://doi.org/10.2514/3.7520

19. Kearney, S. P., Daniel, K. A., Downing, C. R., Lauriola, D. K., Leicht, J., Slipchenko, M., Lynch, K. P., and Wagner, J. L. "100-kHz Coherent Raman Thermometry in a Free-Piston Shock Tube," *Journal of Thermophysics and Heat Transfer*, 2024, pp. 1-7.
https://doi.org/10.2514/1.T6947

20. Jans, E. R., Armstrong, D. J., Smith, A. V., and Kearney, S. P. "Noncolinear optical parametric oscillator for broadband nanosecond pulse-burst CARS diagnostics in gases," *Optics Letters* Vol. 47, No. 7, 2022, pp. 1839-1842.
https://doi.org/10.1364/OL.455526

21. Lynch, K. P., Grasser, T., Spillers, R., Downing, C., Daniel, K., Jans, E., Kearney, S., Morreale, B., Wagnild, R., and Wagner, J. "Design and characterization of the Sandia free-piston reflected shock tunnel," *Shock Waves*, 2023, pp. 1-16.
https://doi.org/10.1007/s00193-023-01127-4

22. Gilvey, J. J., Jans, E. R., Daniel, K. A., Downing, C. R., Lyon, B. T., Lynch, K. P., Wagner, J. L., and Goldenstein, C. S. "High-speed laser-absorption measurements of non-equilibrium nitric oxide in the Sandia Hypersonic Shock Tunnel," *Applied Physics B* Vol. 130, No. 11, 2024, p. 203.
https://doi.org/10.1007/s00340-024-08330-w

23. Howard, M., Bradley, A., Bova, S. W., Overfelt, J., Wagnild, R., Dinzl, D., Hoemmen, M., and Klinvex, A. "Towards performance portability in a compressible cfd code," *23rd AIAA Computational Fluid Dynamics Conference*. 2017, p. 4407.
https://doi.org/10.2514/6.2017-4407

24. McGilvray, M., Jacobs, P. A., Morgan, R. G., Gollan, R. J., and Jacobs, C. M. "Helmholtz resonance of pitot pressure measurements in impulsive hypersonic test facilities," *AIAA Journal* Vol. 47, No. 10, 2009, pp. 2430-2439.
https://doi.org/10.2514/1.42543

25. McBride, B. J. *Computer program for calculation of complex chemical equilibrium compositions and applications*: NASA Lewis Research Center, 1996.

26. Eckbreth, A. C., Dobbs, G. M., Stufflebeam, J. H., and Tellex, P. A. "CARS temperature and species measurements in augmented jet engine exhausts," *Applied Optics* Vol. 23, No. 9, 1984, pp. 1328-1339.
https://doi.org/10.1364/AO.23.001328

27. Smith, A. V. *Crystal nonlinear optics: with SNLO examples*: AS-Photonics Albuquerque, NM, USA, 2018.

28. Michaud, F., Roux, F., Davis, S. P., Nguyen, A.-D., and Laux, C. O. "High-resolution fourier spectrometry of the 14N+ 2 Ion," *Journal of Molecular Spectroscopy* Vol. 203, No. 1, 2000, pp. 1-8.
https://doi.org/10.1006/jmsp.2000.8159

29. Park, C. "Assessment of two-temperature kinetic model for ionizing air," *Journal of thermophysics and heat transfer* Vol. 3, No. 3, 1989, pp. 233-244.
https://doi.org/10.2514/3.28771

30. Kearney, S., Jans, E., Wagner, J., Lynch, K., Daniel, K., Downing, C., Armstrong, D., Wagnild, R., Dechant, L., and Maeng, J. "High-Speed Diagnostic and Simulation Capabilities for Reacting Hypersonic Reentry Flows: LDRD Final Report." Sandia National Lab.(SNL-NM), Albuquerque, NM (United States), 2022.

31. Park, C. *Nonequilibrium hypersonic aerothermodynamics*: Wiley, 1990.

32. Kleine, H., Lyakhov, V., Gvozdeva, L., and Grönig, H. "Bifurcation of a reflected shock wave in a shock tube," *Shock Waves: Proceedings of the 18th International Symposium on Shock Waves, Held at Sendai, Japan 21–26 July 1991*. Springer, 1992, pp. 261-266.
https://doi.org/10.1007/978-3-642-77648-9_36

33. Millikan, R. C., and White, D. R. "Systematics of vibrational relaxation," *The Journal of chemical physics* Vol. 39, No. 12, 1963, pp. 3209-3213.
https://doi.org/10.1063/1.1734182

34. Kim, M. K., Esser, B., Koch, U., and Guelhan, A. "Numerical and experimental study of high enthalpy flows in a hypersonic plasma wind tunnel: L3K," *42nd AIAA Thermophysics Conference*. 2011, p. 3777.
https://doi.org/10.2514/6.2011-3777

35. Park, C. "Review of chemical-kinetic problems of future NASA missions. I-Earth entries," *Journal of Thermophysics and Heat transfer* Vol. 7, No. 3, 1993, pp. 385-398.
https://doi.org/10.2514/3.431

36. Streicher, J. W., Krish, A., and Hanson, R. K. "High-temperature vibrational relaxation and decomposition of shock-heated nitric oxide: II. Nitrogen dilution from 1900 to 8200 K," *Physics of Fluids* Vol. 34, No. 11, 2022.
https://doi.org/10.1063/5.0122787

37. Taylor, R., Camac, M., and Feinberg, R. "Measurements of vibration-vibration coupling in gas mixtures," *Symposium (International) on Combustion*. Vol. 11, Elsevier, 1967, pp. 49-65.
https://doi.org/10.1016/S0082-0784(67)80133-4

38. Lee, S., Kim, I., Park, G., Lee, J. K., and Kim, J. G. "Thermochemical nonequilibrium flow analysis in low enthalpy shock-tunnel facility," *PloS one* Vol. 15, No. 10, 2020, p. e0240300.
https://doi.org/10.1371/journal.pone.0240300